

Proof of Concept of an Iron-Iron(III)oxide hydroxide Battery Working at Neutral pH

C. Gutsche*, S. Berling, T. Plaggenborg, J. Parisi, M. Knipper

University of Oldenburg, Department of Physics, Energy and Semiconductor Research Laboratory,
Carl-von-Ossietzky Str. 9-11, 26129 Oldenburg, Germany

*E-mail: Christian.gutsche@uni-oldenburg.de

Received: 12 February 2018 / Accepted: 8 November 2018 / Published: 5 January 2019

An iron-iron(III)oxide hydroxide battery working in a neutral pH range is introduced. It employs electrochemical deposition of metallic Fe at the negative electrode and Fe^{III}OOH at the positive electrode during charge and dissolution of both during discharge in an aqueous Fe^{II} electrolyte. The working principle was validated with cyclic voltammetry, charge-discharge cycles, weighing, profilometry, X-ray diffraction, scanning electron microscopy, and energy dispersive X-ray analysis. The coulombic efficiency over seven cycles is (49 ± 5) %, while it is (40 ± 2) % for the voltaic efficiency and (20 ± 1) % for the overall efficiency using current densities for charging and discharging of 1.2 mA cm⁻² and 0.4 mA cm⁻² at the negative electrode and 24 μA cm⁻² and 8 μA cm⁻² at the positive electrode. .

Keywords: Lepidocrocite; Low-cost battery; Neutral electrolyte; Fe^{II}; FeOOH

1. INTRODUCTION

A crucial challenge concerning the transition towards a sustainable energy system is the development of low-cost batteries. For residential storage systems, a high energy density is not as important as for mobile applications.[1] This offers opportunities to decrease costs by choosing low-cost materials. Since iron (Fe) is highly abundant and by far the cheapest metal, a battery with both electrodes being Fe based might enable significantly cheaper energy storage – given the low overall material and production costs as well as a sufficient efficiency and stability. There are already completely Fe based redox flow batteries working at acidic and alkaline pH. In terms of cost, the redox flow battery design is more suited to large-scale batteries than for residential applications due to the low costs for scaling up the electrolyte tanks, and the relatively high costs of the stack.[2-5] Inspired by the Pourbaix diagram of the Fe system [6], we herein present a completely Fe-based battery

working in the neutral pH range and having a simple, and thus cheap, design. Since this system avoids the use of heavy metals and too high or too low pH values, and works with an aqueous electrolyte that has a comparably low energy density, its risk potential is relatively low.

The battery consists of an Fe-based electrode, an Fe^{III}OOH-based electrode, and an aqueous electrolyte with soluble Fe^{II} species. During charge, the Fe^{II} is reduced to metallic Fe at the negative electrode and oxidized to deposit as Fe^{III}OOH on the positive electrode. During discharge, both deposits are electrochemically dissolved (Fig. 1). Deposition and dissolution of both single electrodes are known from the literature, e.g. from the fields of corrosion science or electrodeposition of precursors for photoelectrodes for solar water splitting. [7-17]

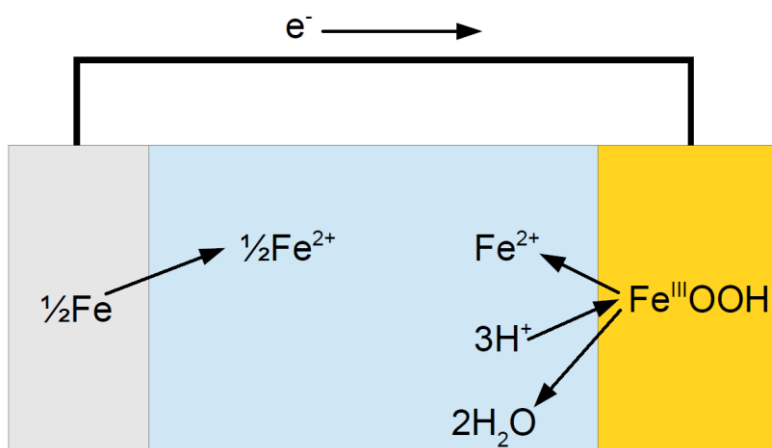
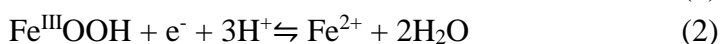


Figure 1. Sketch of the battery's working principle for the discharge case.

The soluble Fe^{II} can be present in different forms: According to the literature, the solubility of Fe(OH)₂ is negligible as well as the concentration of FeCl⁺ in solution.[18] Other possible Fe^{II} species are Fe²⁺ and FeOH⁺. Their ratio is described by the hydrolysis constant $\beta = ([\text{FeOH}^+][\text{H}^+]) / ([\text{Fe}^{2+}][\text{H}_2\text{O}])$ using the simplifying assumption of an activity of 1.[18-20] At a pH of 7, $[\text{H}^+] = 10^{-7} \text{ mol l}^{-1}$. According to the literature, $\beta = 3.1 \cdot 10^{-10}$. [19,20] This yields an $[\text{FeOH}^+]:[\text{Fe}^{2+}]$ ratio of 0.17 at a pH of 7. So, Fe²⁺ is assumed to be the dominant species in the electrolyte in accordance with the literature.[21] For the sake of simplicity, we do not include the hydration shell in the nomenclature, and use Fe²⁺ instead of Fe(H₂O)₆²⁺. The proposed electrode reactions are



The aim of our work is to provide proof of concept of the battery. Therefore, the deposition and dissolution of the Fe^{III}OOH at the positive electrode, and of Fe at the negative electrode were investigated via weighing, profilometry, scanning electron microscopy (SEM), energy dispersive X-ray (EDX) spectroscopy, and X-ray diffraction (XRD), and were compared to the electrochemical data. Cyclic voltammograms (CVs) as well as charge-discharge cycles were recorded, and the efficiencies were calculated.

2. EXPERIMENTAL

60 ml of the electrolyte were prepared using de-ionized water purged with inert gas with 1 M NaCl (VWR, 99.9%) and 0.2 M FeCl₂ xH₂O (99%, Alfa Aesar, reagent grade) because it is known from the literature that chloride ions reduce hydrogen evolution and maximize Fe plating at the negative electrode and facilitate the FeOOH deposition at the positive electrode compared to a sulfate electrolyte.[17,22] 0.05 M 1-methylimidazole (99%, Sigma Aldrich, purity > 98.5%) was used as buffering agent. All chemicals were used without further purification. The pH value measured before and after the electrochemical measurements was pH 7.

All electrochemical measurements were performed at room temperature under inert gas flow using a Solartron Modulab potentiostat. A steel mesh with a wire diameter of $d = 0.12$ mm and a mesh size of $M = 0.25$ mm and a geometric area of 12.5 cm² was used as positive electrode. A microscope slide coated with a Au layer served as negative electrode. It was isolated with nail polish except an active area of 0.25 cm² and the upper end, where it was electrically contacted. The electrode potentials were measured against a silver/silver chloride (Ag/AgCl) reference electrode. Electronic iR compensation was applied.

The film thickness was measured with a stylus profiler (Veeco Dektak 6M) with a 12.5 μm stylus and a bearing force of 15 mg. SEM images and EDX spectroscopic data were taken with a combined FIB-SEM system (Helios NanoLab 600i, FEI) with an acceleration voltage of 30 kV and a current of 11 nA. XRD measurements were conducted using a PANalytical X'Pert Pro powder X-ray diffractometer operating with Cu Kα radiation in Bragg–Brentano θ – θ geometry, using an automatic divergence slit. Reference data were taken from the database of the International Centre for Diffraction Data (ICDD 2009).

3. RESULTS AND DISCUSSION

3.1 Fe Electrode

In the electrolyte, a dark precipitate was observed that is likely Fe(OH)₂ with traces of Fe^{III} that was produced via oxidation by traces of oxygen.[18] However, electrochemical experiments with the soluble Fe^{II} species could be well conducted. Fig. 2a shows CVs of the negative Au electrode with varying lower potential limits E_{\min} . In the cathodic scan at potentials lower than -0.9 V vs. Ag/AgCl the Fe deposition feature evolves. One can see the current crossing that is typical for electrodeposition in the black CV in Fig. 2a marked with “A”. It is due to a nucleation overpotential at the beginning of the electrodeposition that also leads to a steep onset of the cathodic peak. At potentials more negative than -1 V vs. Ag/AgCl, hydrogen evolution dominates. This is in accordance with the decrease of the anodic charge (related to Fe stripping) normalized to the cathodic charge (that is mainly Fe deposition in the black CV and to a significant amount hydrogen evolution in the red CV): The ratio of anodic to cathodic charge is 0.85 in the case of the black CV and 0.69 in the case of the red CV due to hydrogen evolution. This might give a hint to coulombic efficiencies of the negative electrode reactions in the

battery. In the red CV in Fig. 2a with a lower potential limit of -1.2 V vs. Ag/AgCl, two new anodic features evolve at around -0.55 V vs. Ag/AgCl (marked with “B”) and -0.45 V vs. Ag/AgCl (marked with “C”). Both are likely related to the stripping of Fe atoms with altered binding energies due to the influence of the hydrogen, the locally lower pH due to hydrogen evolution, or the more negative potentials that were applied in the CV.

At the negative electrode, hydrogen evolution occurs as an unintended side reaction as also shown in the literature at lower pH values.[17] That might decrease the charge efficiency of the battery, if the potential applied at the negative electrode is too negative. To study the deposition during charging and the dissolution during discharging, the battery was charged for 2 h with $i = 300 \mu\text{A}$, left at open circuit for ten minutes and discharged with $i = -100 \mu\text{A}$ until the cell voltage reached 0.1 V (Fig. 2c). That translates into current densities per geometric electrode area of 1.2 mA cm^{-2} and 0.4 mA cm^{-2} at the Au substrate as negative electrode and $24 \mu\text{A cm}^{-2}$ and $8 \mu\text{A cm}^{-2}$ at the steel mesh that served as positive electrode. The current densities at the negative electrode are, thus, comparable to the typical 1 mA cm^{-2} in lithium ion batteries.[23] In order to minimise voltaic efficiency losses due to a nucleation overpotential the negative electrode area was chosen to be relatively small. In contrast to that, the positive electrode was chosen to have a relatively large surface area in order to minimise the current densities, and thus the voltaic losses during electrodeposition and electrodisolution. For the sake of reproducibility, three pairs of electrodes that had been charged, and three pairs that had been charged and subsequently discharged, were studied. In Fig. 2c, the potentials at the positive and negative electrode E_{pos} and E_{neg} , as well as the cell voltage U_{cell} and the current i are shown as function of time.

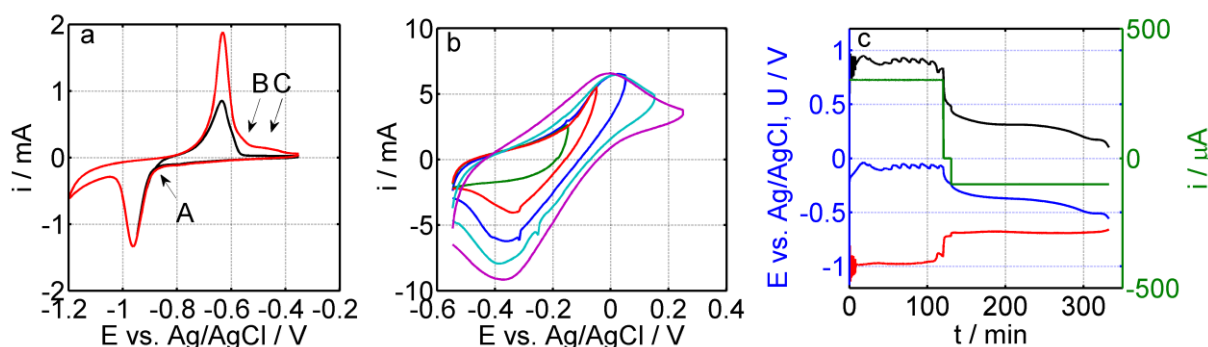


Figure 2. CVs at the negative (Au) electrode recorded with 100 mV s^{-1} , an upper potential limit of -0.35 V vs. Ag/AgCl, and varying lower potential limits showing Fe deposition and subsequent Fe stripping (a). CVs of the positive (steel mesh) electrode performed with 100 mV s^{-1} . The lower potential limit is -0.55 V vs. Ag/AgCl. They show with increasing upper potential limit the evolution of the oxidative feature and, consequently, of the reduction signal (b). One charge-discharge cycle consisting of 2 hours of charging with a current $i = 300 \mu\text{A}$, 10 minutes open circuit, and discharge with $i = 100 \mu\text{A}$ until the cancelation criterion (cell voltage $U_{\text{cell}} < 0.1$ V) was met. The potential evolution at the positive electrode (blue) and the negative electrode (red), as well as the cell voltage (black) and the current (green) are shown (c).

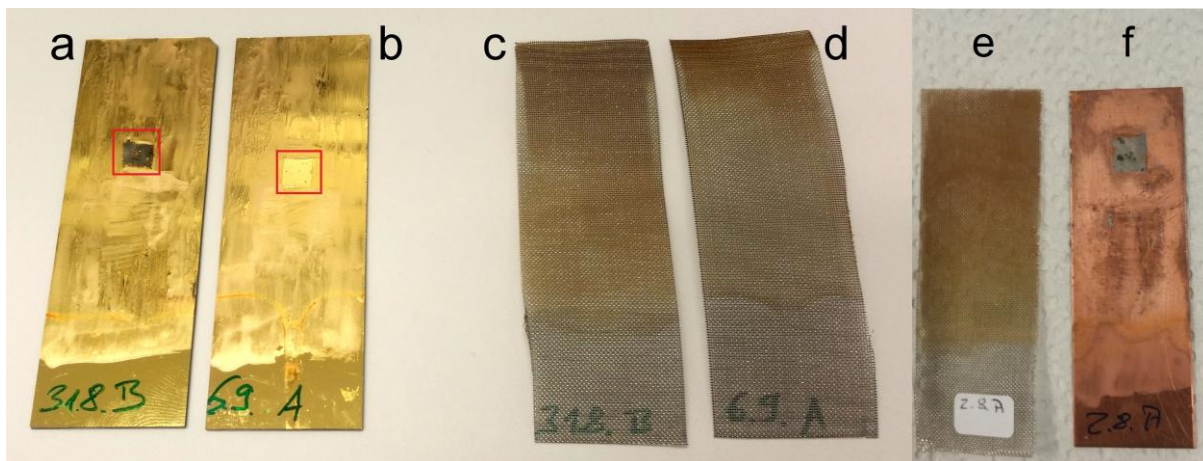


Figure 3. Photographs of the negative Au electrode after charging (a) showing deposition of Fe, after discharging (b) showing total dissolution of Fe (active area marked red), of the positive steel mesh electrode after charging (c) and discharging (d), both showing brownish FeOOH electrodeposits. Photograph of a steel mesh (e) and a Cu electrode (f) after electrodeposition of FeOOH and Fe as conducted with the Au electrode. The metallic Fe deposit as well as small dark areas are clearly observable on the Cu electrode.

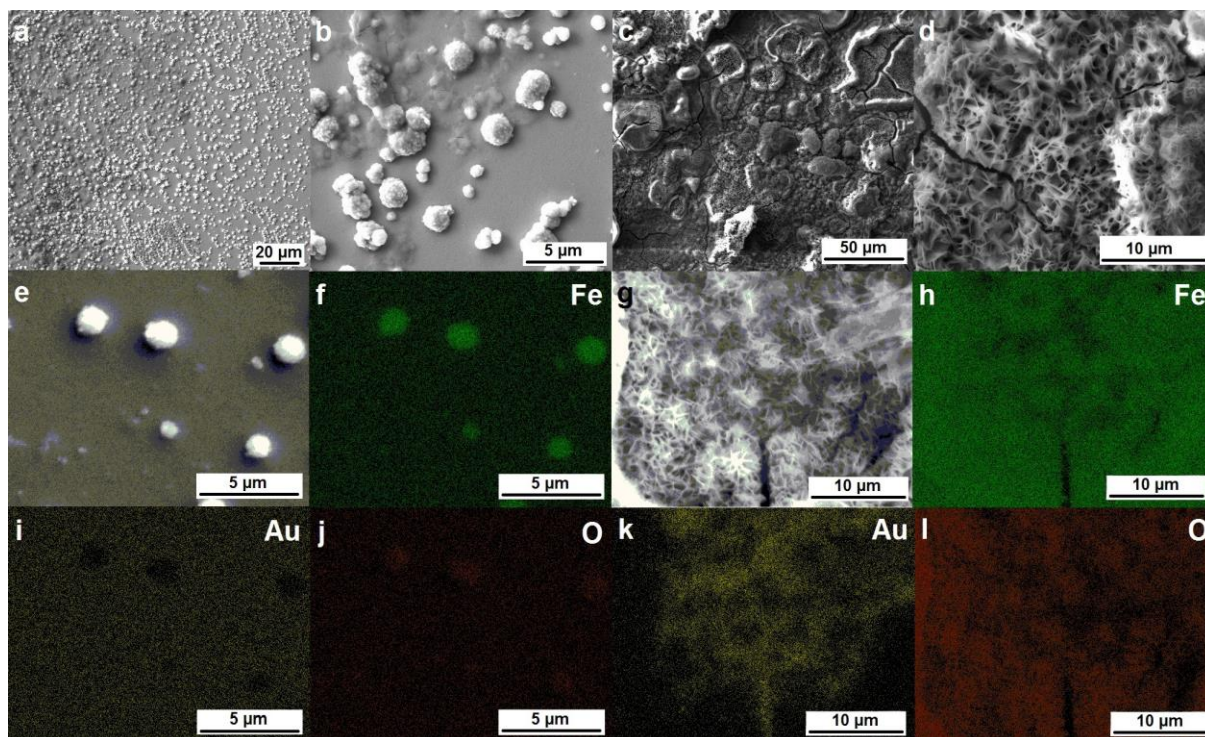


Figure 4. Survey (a) and detail (b) SEM image of the metallic Fe deposit and EDX spectroscopic maps of the elements Fe (f), Au (i), and O (j) of the area shown in the SEM image (e). Survey (c) and detail (d) SEM image of the dark Fe deposit and EDX spectroscopic maps of the elements Fe (h), Au (k), and O (l) of the area shown in the SEM image (g). The EDX measurements prove that the deposits contain Fe, accompanied by a small amount of O likely due to oxidation of the samples on air. They also show: the more Fe, the less Au is detectable.

Potential fluctuations were observed in some of the measurements during charging on both electrodes differing in the amplitude of the potential variation and the temporal expansion. In the open circuit phase, the negative electrode's potential equilibrated quite quickly, indicating a not too porous structure, while the potential equilibration was not finished by the positive electrode at the end of the open circuit phase, probably due to hindered diffusion in a highly porous deposit. Noteworthy is the low overpotential for Fe dissolution.

The coulombic, voltaic and energy efficiencies estimated from the charge-discharge cycle are: $\eta_{\text{coul}} = 56 \%$, $\eta_{\text{volt}} = 32 \%$, and $\eta_{\text{energy}} = 18 \%$.

The electrodeposited Fe on the Au substrate after charging and its redissolution after discharging is clearly observable in Fig. 3a and b. A metallic deposit and in some cases a small amount of a dark deposit can be observed on the charged electrodes, both differing in nanostructure as shown in Fig. 4 and in thickness.

In the metallic looking region, EDX measurements prove the deposition of Fe on the entire electrode. Additionally nodular Fe deposits with a typical diameter of one to two micrometers can be observed. The typical film thickness measured via profilometry is of the order of some hundreds of nanometers. In the dark region, the typical film thickness is in the range of a few micrometers. The larger layer thickness of the dark deposit indicates a higher mass being deposited indicating a higher current density during charging at this area. According to Faraday's law, the transported charge of 2160 mC translates into 11.4 μmol of Fe deposited. With a molar mass of $M_{\text{Fe}} = 56 \text{ g mol}^{-1}$ and a density of $\rho_{\text{Fe}} = 7.9 \text{ g cm}^{-3}$ [24] the expected mass of the deposit is 636 μg and a mean thickness of 3.0 μm assuming a non-porous deposit.

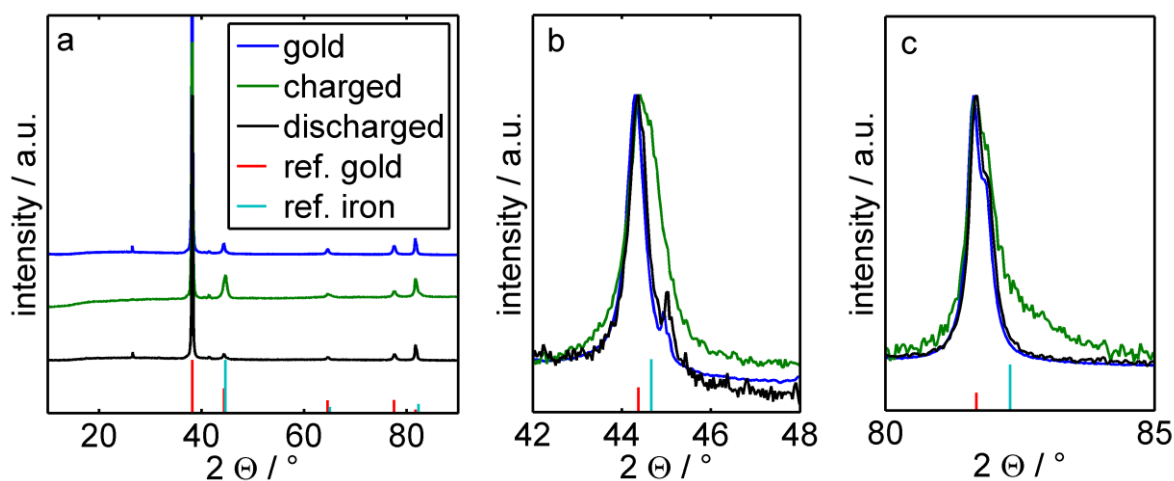


Figure 5. XRD patterns of the untreated Au sample (blue), the sample after charging (green) and after charging and discharging (black). The stick patterns show the reference patterns of Au (ICDD number 03-065-8601) and Fe (ICDD number 03-065-4899). A closer look at the selected reflections indicates the presence of Fe after charging and its redissolution after discharging.

In the case of a deposition efficiency of 50 % due to hydrogen evolution, the mean thickness would decrease to 1.5 μm . So, the measured thickness is in agreement with the calculation. The dark

deposit is heavily nanostructured consisting of elongated structures with a thickness in the range of 100 nm. The dark colour of the deposit can be explained as a consequence of the nanostructuring.[25] The dark colour and the SEM images indicate smaller crystallites than in the metallic looking areas, indicating a higher current density than in the regions where metallic looking Fe has been deposited. A small amount of oxygen can also be observed via EDX spectroscopy likely originating from the oxidation of Fe on air.

After discharge, no Fe is visible at the Au electrode (Fig. 3b). Due to the similarity of the lattices of Au and Fe, their XRD features overlap, making analysis more challenging. However, the existence of Fe features at higher angles are clearly observable after charging and disappear after discharging (Fig. 5) in accordance with the expectations and the other measurements.

3.2 Iron(III)oxide hydroxide Electrode

CVs of the FeOOH electrode are shown in Fig. 2b. The redox potential is around -0.2 V vs. Ag/AgCl. In the anodic scan, Fe^{2+} ions are oxidised to $\text{Fe}^{\text{III}}\text{OOH}$, in the cathodic scan, this is reduced back to Fe^{2+} . With increasing upper potential limit, the anodic charge increases, and thus so does the cathodic feature, since only species that were previously electrodeposited can later be reduced.

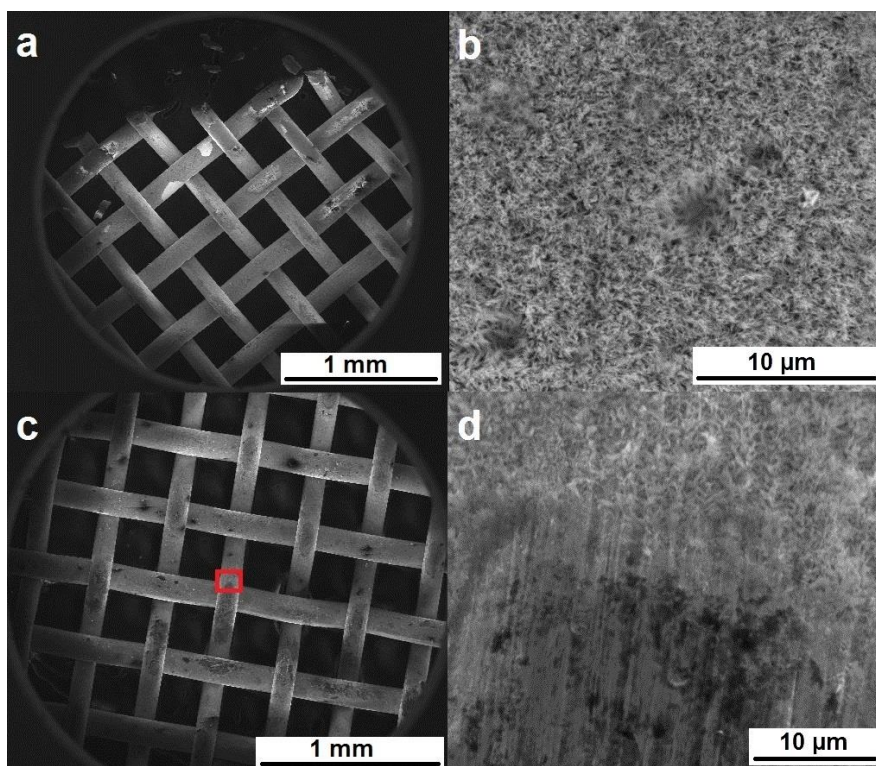


Figure 6. SEM images of steel mesh after charging (a). The bright areas originate from NaCl. A closer look reveals the deposit's nanostructure (b). SEM images of steel mesh after charging and discharging (c). The darker areas originate from pure steel after FeOOH dissolution. A transition from blank steel to FeOOH is marked in red and shown in detail in (d).

The deposition of a brownish compound is visible in Fig. 3c and d. On this steel mesh substrate, a differentiation between the charged and discharged sample by the eye alone was not easily possible. However, weighing allowed the estimation of a mass increase of the steel electrodes after charging of $\Delta m = (1.8 \pm 0.2)$ mg. This value is in good agreement with the expected mass increase of 2.0 mg according to Faraday's law ($22.8 \mu\text{mol FeOOH}$ with $M_{\text{FeOOH}} = 89 \text{ g mol}^{-1}$). The mass increase after charging and subsequent discharging is $\Delta m = (0.8 \pm 0.4)$ m, which is significantly lower than after charging, thus validating the deposition and subsequent dissolution of FeOOH. The mass difference in the order of 50 % fits well to the observed coulombic efficiencies in the order of 50 %.

These findings were strengthened by XRD, SEM, and EDX measurements. SEM images show a relatively uniform deposition of a nanostructured Fe compound. After discharge, darker areas appeared as a result of dissolution of the Fe compound and the consequent uncovering of the steel substrate (Fig. 6). This is validated by the variation of the O signal in the EDX image (Fig. 7). According to the weight difference, on average, half the material should have been redissolved, meaning not only an uncovering of the steel, but also a thinning of the Fe compound.

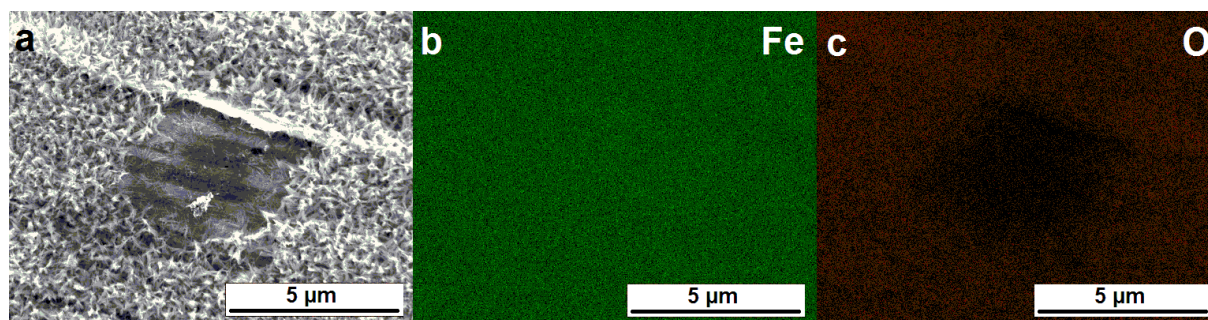


Figure 7. SEM image of an area showing FeOOH deposit as well as the underlying steel after discharging (a). Fe EDX map showing a uniform Fe distribution (b). O EDX map showing a higher amount of O within the FeOOH deposit than on the bare steel (c).

XRD measurements were performed in order to estimate the phase of the Fe compound that was anodically deposited from the Fe^{2+} electrolyte (Fig. 8). In order to differentiate between XRD signals due to the deposition of the Fe compound from the Fe^{2+} ions containing electrolyte and due to a possible (electro)chemical treatment of the steel mesh, $-0.1 \text{ V vs. Ag/AgCl}$ were applied to the steel mesh in an Fe-free electrolyte and the XRD results were compared to those from the untreated mesh, as well as those from the charged and discharged electrode. The mean current during this 2 h oxidative treatment was $-1 \mu\text{A}$, meaning a total charge of $-2 \mu\text{Ah}$. After oxidising the steel mesh for two hours all steel reflections lost intensity without broadening. This means that the crystallite size did not decrease significantly. Three strong features appeared at 44.7° , 65.0° , and 82.2° . Together with the evolving feature at 98.8° , they can be attributed to Fe domains that might have developed as a result of leaching or dealloying of the steel. The formation of the Fe can explain the decrease of the initial steel signal. Three reflections appeared between 10° and 20° . The origin of the second and third signal is unclear. The first one can be assigned to lepidocrocite, $\gamma\text{-FeOOH}$. After charging, all lepidocrocite reflections can be observed in accordance with the literature.[10] After the discharge, an intensity

decrease of all signals except the one at around 14° can be noted caused by the electrodisolution of the lepidocrocite as reported in the literature.[12] Moreover, after discharge the original steel signals became more pronounced, again. This can also be explained by the dissolution of the lepidocrocite.

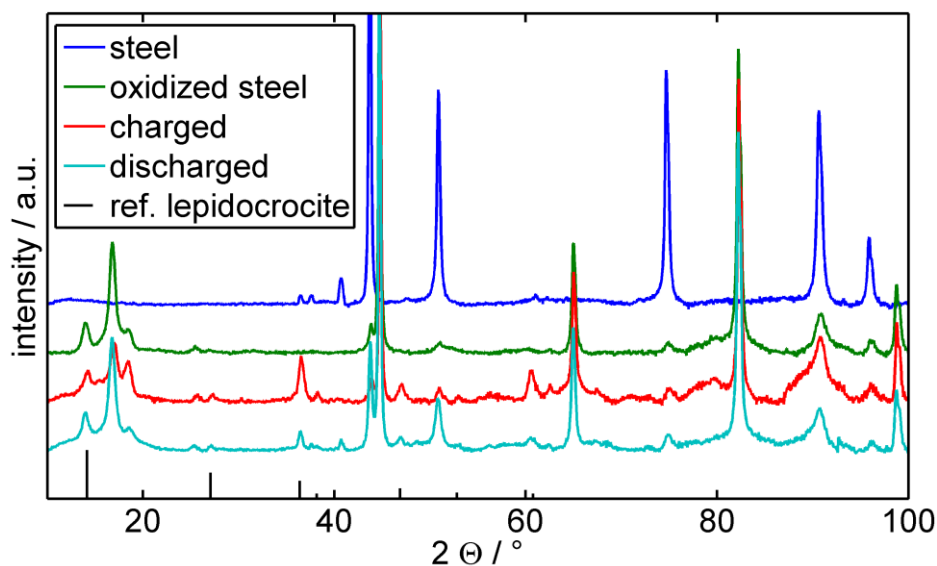


Figure 8. XRD patterns of untreated steel (blue), steel after 2 hours of oxidation at -0.1 V vs. Ag/AgCl (green), after charging (red) and after charging and discharging (light blue). The stick pattern shows the reference pattern of lepidocrocite (ICDD number 01-074-1877). The appearance and decline of the lepidocrocite reflections indicate its deposition and dissolution.

3.3 Charge Discharge Cycles

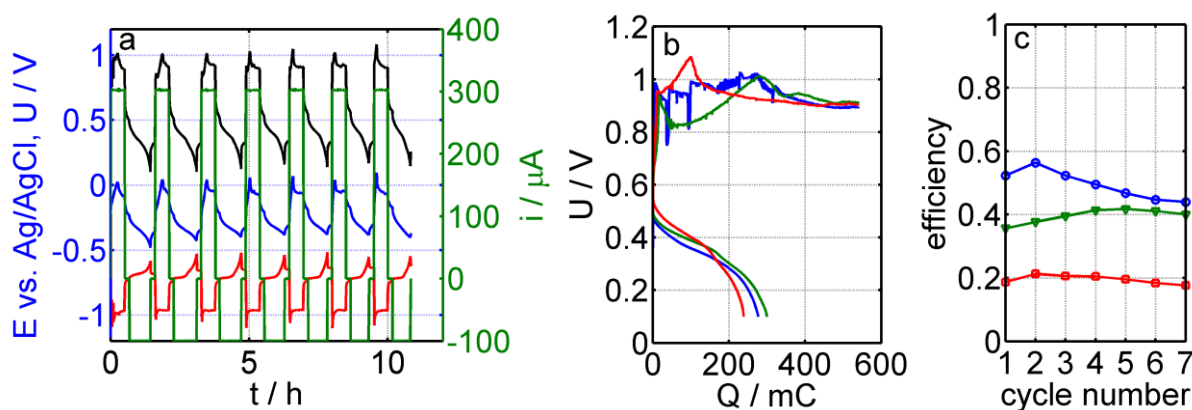


Figure 9. Current (green), cell voltage (black), and potential at the positive (blue) and negative (red) electrode as function of time during seven charge-discharge cycles (a). Cell voltage behaviour during charge and discharge for the first (blue), third (green) and seventh cycle (red). The voltage variations in the first cycle originate from the negative electrode (b). The coulombic (blue), voltaic (green), and energy efficiency (red) as a function of the cycle number (c).

In Fig. 9a, the current, cell voltage and the potential at the positive and negative electrode are shown as a function of time during seven charge-discharge cycles. The battery was charged with 300 μA for 30 minutes and discharged with -100 μA until the cell voltage dropped to 0.1 V. The charge and discharge steps are separated by 10 minutes of open circuit.

The mean of the charging voltage over all cycles is 0.91 V, for the discharging it is 0.36 V. Voltage curves of selected cycles are shown in Fig. 9b. The variation of the voltage behaviour during discharge between the cycles was relatively low. The voltage behaviour during charging was dominated by the potential maximum at the positive electrode and reaches 0.9 V at the end of the charging phase. In the open circuit phase after charging, the negative electrode's potential equilibrated relatively quickly, indicating a not too porous structure of the deposit, while the potential equilibration had not finished at the positive electrode by the end of the open circuit phase, probably due to hindered diffusion in a highly porous deposit. After discharge, the equilibrium potential was reached faster on both electrodes. The open circuit potentials after charging and after discharging differed by roughly 60 mV at the negative electrode and by roughly 140 mV at the positive one. Therefore, the overpotentials during charge and discharge at both electrodes, which were used to estimate the contributions to the voltaic efficiency loss, were defined with respect to the last value of the previous open circuit phase. The overpotential of the Fe electrode during charging was in the range of 300 mV. Despite an initially higher overpotential likely due to nucleation the potential was stable. The discharge overpotential was in the range of 20 mV and was stable for roughly half the discharge time. Then it rose, probably because the electrode area covered with Fe decreased. The overpotential of the FeOOH electrode for charging was at the beginning in the range of 150 mV and increased rapidly until it reached a maximum at a potential 400 mV more positive than the open circuit potential, stabilising at a potential of around 100 mV less positive than the maximum value. The initial discharge overpotential was in the range of 60 mV, but during discharge it was relatively constantly falling. The coulombic efficiency was governed by the Fe electrode showing a steeper potential change before the cancellation criterion of $U_{\text{cell}} = 0.1$ V was reached. This was not unexpected, since hydrogen evolution occurs as a side reaction to Fe deposition, thus lowering the deposition efficiency and, consequently, the battery's coulombic efficiency.

The mean and standard deviation of the coulombic efficiency over the seven cycles was (49 ± 5) %, while it was (40 ± 2) % for the voltaic efficiency and (20 ± 1) % for the overall efficiency. The efficiencies of the first cycles were a little bit lower than those of the second one. After that, the voltaic efficiency rose and stabilised in the range of 40 %, while the coulombic efficiency continuously decreased. Consequently, the energy efficiency decreased slowly from the second to the seventh cycle (Fig. 9c).

The voltaic efficiency η_{volt} is related to losses at both electrodes during charge as well as during discharge. The contributions to the voltaic efficiency loss $\Delta\eta_{\text{pos,discharge}}$, $\Delta\eta_{\text{neg,discharge}}$, $\Delta\eta_{\text{pos,charge}}$, and $\Delta\eta_{\text{neg,charge}}$ were calculated by using the single electrode potentials shown in Fig. 10a. They are defined as:

$$\eta_{\text{volt}} = 1 - (\Delta\eta_{\text{pos,discharge}} + \Delta\eta_{\text{neg,discharge}} + \Delta\eta_{\text{pos,charge}} + \Delta\eta_{\text{neg,charge}}) \quad (3)$$

and calculated by using the single electrode potentials E_{pos} and E_{neg} and the difference between both, the cell voltage U . The calculation of the partial contributions to the voltaic efficiency losses is based on the single electrode potentials. For charge and discharge, the averaged potentials $E_{\text{pos,discharge}}$, $E_{\text{neg,discharge}}$, $E_{\text{pos,charge}}$, and $E_{\text{neg,charge}}$ were used. As open circuit potentials $E_{\text{pos,OC}}$ and $E_{\text{neg,OC}}$ the values at the end of the open circuit phase were taken. Consequently, the single overpotentials $\Delta E_{\text{pos,discharge}}$, $\Delta E_{\text{neg,discharge}}$, $\Delta E_{\text{pos,charge}}$, and $\Delta E_{\text{neg,charge}}$ were defined as difference between the averaged charge or discharge potential and the open circuit potential at each electrode. With these defined parameters the voltage efficiency can be expressed as:

$$\eta_{\text{volt}} = (U_{\text{discharge}}) / (U_{\text{charge}}) \quad (4)$$

$$= (U_{\text{OC}} - \Delta E_{\text{pos,discharge}} - \Delta E_{\text{neg,discharge}}) / (U_{\text{OC}} + \Delta E_{\text{pos,charge}} + \Delta E_{\text{neg,charge}}) \quad (5)$$

For the further calculation, the overpotentials are normalized to the cell's open circuit voltage U_{OC} and named $\Delta E_{\text{pos,dis,n}}$, $\Delta E_{\text{neg,dis,n}}$, $\Delta E_{\text{pos,cha,n}}$, $\Delta E_{\text{neg,cha,n}}$. This allows the following reformulation:

$$\eta_{\text{volt}} = (1 - \Delta E_{\text{pos,dis,n}} - \Delta E_{\text{neg,dis,n}}) / (1 + \Delta E_{\text{pos,cha,n}} + \Delta E_{\text{neg,cha,n}}) \quad (6)$$

The single contributions $\Delta \eta_i$ (meaning $\Delta \eta_{\text{pos,discharge}}$, $\Delta \eta_{\text{neg,discharge}}$, $\Delta \eta_{\text{pos,charge}}$, and $\Delta \eta_{\text{neg,charge}}$) can be calculated using the normalized overpotentials $\Delta E_{i,n}$ (meaning $\Delta E_{\text{pos,dis,n}}$, $\Delta E_{\text{neg,dis,n}}$, $\Delta E_{\text{pos,cha,n}}$, $\Delta E_{\text{neg,cha,n}}$) via:

$$\Delta \eta_i = \eta_{\text{volt}}(\Delta E_{i,n=0}) - \eta_{\text{volt}}(\Delta E_{i,n}) \quad (7)$$

That simplifies to:

$$\Delta \eta_{\text{pos,discharge}} = \Delta E_{\text{pos,dis,n}} / (1 + \Delta E_{\text{pos,cha,n}} + \Delta E_{\text{neg,cha,n}}) \quad (8)$$

$$\Delta \eta_{\text{neg,discharge}} = \Delta E_{\text{neg,dis,n}} / (1 + \Delta E_{\text{pos,cha,n}} + \Delta E_{\text{neg,cha,n}}) \quad (9)$$

$$\Delta \eta_{\text{pos,charge}} = [(1 - \Delta E_{\text{pos,dis,n}} - \Delta E_{\text{neg,dis,n}}) \Delta E_{\text{pos,cha,n}}] / [(1 + \Delta E_{\text{neg,cha,n}}) (1 + \Delta E_{\text{pos,cha,n}} + \Delta E_{\text{neg,cha,n}})] \quad (10)$$

$$\Delta \eta_{\text{neg,charge}} = [(1 - \Delta E_{\text{pos,dis,n}} - \Delta E_{\text{neg,dis,n}}) \Delta E_{\text{neg,cha,n}}] / [(1 + \Delta E_{\text{pos,cha,n}}) (1 + \Delta E_{\text{pos,cha,n}} + \Delta E_{\text{neg,cha,n}})] \quad (11)$$

The partial contributions were calculated for the single charge-discharge cycles, normalised to the sum of partial contributions and then averaged over the number of measured cycles. Due to the difference of the open circuit potential after charging and discharging, there was an error in the estimation of the partial contributions. However, the calculation allows a rough evaluation of the effect of the mentioned processes. The voltaic losses originate to $(36 \pm 3) \%$ from the charging of the

negative electrode, to (29 ± 3) % from the charging of the positive electrode, to (25 ± 2) % from the discharging of the positive electrode, and to (10 ± 1) % from the discharging of the negative electrode. The contribution of the losses due to charging at the negative electrode slightly increased during cycling, the contribution of the discharging at the positive electrode remained constant, whereas the other contributions slightly decreased.

Comparing the efficiency values of this battery to other batteries is not an easy task because of the different working principles. Moreover, it is obvious that initial studies do not yield the efficiencies of later studies that are based on a deeper investigation of the battery's loss mechanisms and further optimisation. However, the most comparable batteries are a Pb-PbO₂ redox flow battery developed in the Pletcher group at Southampton and a totally Fe based acidic redox flow battery from the Savinell group.[2,26] Although our battery is not a redox flow battery it might in principle be operated like the Pb-PbO₂ one. Comparing these batteries with the Fe-FeOOH battery one should keep in mind that the electrolyte flow allows higher current densities and reduces overpotentials due to diffusion limitation. Pletcher's group estimated the efficiency of a Pb-PbO₂ redox flow battery by measuring the electrochemical properties of the reactions at both electrodes at elevated temperatures while they were rotated. The results are based on three cycles each lasting roughly 20 minutes. They achieved an energy efficiency of 70 %. A first study of a completely Fe based acidic redox flow battery working at elevated temperatures lead to an average energy efficiency of around 30 % over 60 cycles at during which 13 actions were undertaken in order to maintain or increase the efficiency. The charging current of 300 μ A and the discharging current of 100 μ A yield current densities per geometric electrode area of 1.2 mA cm⁻² and 0.4 mA cm⁻² at the Au substrate (the negative electrode) and 24 μ A cm⁻² and 8 μ A cm⁻² at the steel mesh that served as positive electrode. The current densities at the negative electrode are, thus, comparable to the typical 1 mA cm⁻² in lithium ion batteries.[23] The use of catalysts for increasing the efficiencies as well as current densities of the FeOOH deposition and dissolution will be studied in future work. The use of solid or soluble catalysts related to the electrodeposition and -dissolution of electrode materials in batteries is known e.g. from lithium-oxygen batteries or from a Pb-PbO₂ flow battery, where PbO₂ is electrodeposited and -dissolved in a Pb²⁺ electrolyte.[26-30] The use of hydrogen evolution suppressors might be helpful in order to minimise losses due to hydrogen evolution.

4. CONCLUSIONS

We have introduced a novel iron-iron(III)oxide hydroxide battery, that works in a neutral pH range. It employs electrochemical deposition and dissolution of metallic Fe at the negative electrode and of Fe^{III}OOH at the positive electrode during charge and discharge in an Fe^{II} electrolyte. The electrodeposition and dissolution of the Fe and FeOOH deposit was validated via XRD, SEM, EDX, weighing, and profilometry. A mean energy efficiency of (20 ± 1) % is reported over seven cycles. In order to raise the system's efficiency future studies should investigate in more detail the charge and discharge processes at both electrodes. Some approaches that might help are the use of solid or soluble

catalysts for the deposition and dissolution of the positive electrode and hydrogen evolution suppressors.

ACKNOWLEDGEMENTS

The authors gratefully acknowledge funding by EWE AG Oldenburg. Thanks to C. Ponce de León and R. McKerracher from the University of Southampton for fruitful discussion.

References

1. A. S. Grigoriev, V. V. Skorlygin, S. A. Grigoriev, D. A. Melnik and M. N. Filimonov, *Int. J. Electrochem. Sci.*, 13 (2018) 1822.
2. L.W. Hruska and R.F. Savinell, *J. Electrochem. Soc.*, 128 (1981) 18.
3. J.R. Goldstein, Novel flow battery and usage thereof, US20150048777 A1, 2015. <http://www.google.ch/patents/US20150048777> (accessed April 20, 2017).
4. M.C. Tucker, A. Phillips and A.Z. Weber, *ChemSusChem.*, 8 (2015) 3996.
5. J. Sassen, Novel iron anode for stationary storage, WO2016193963 A1, 2016. <http://www.google.com/patents/WO2016193963A1> (accessed April 20, 2017).
6. M. Pourbaix, Atlas of electrochemical equilibria in aqueous solutions, Pergamon, Oxford, 1966.
7. S. Peulon, H. Antony, L. Legrand and A. Chausse, *Electrochim. Acta*, 49 (2004) 2891.
8. S. Peulon, L. Legrand, H. Antony and A. Chaussé, *Electrochem. Commun.*, 5 (2003) 208.
9. H. Antony, S. Peulon, L. Legrand and A. Chaussé, *Electrochim. Acta*, 50 (2004) 1015.
10. L. Martinez, D. Leinen, F. Martín, M. Gabas, J.R. Ramos-Barrado, E. Quagliata and E.A. Dalchiele, *J. Electrochem. Soc.*, 154 (2007) D126.
11. H. Antony, L. Legrand and A. Chaussé, *Electrochim. Acta*, 53 (2008) 7146.
12. H. Antony, L. Legrand, L. Maréchal, S. Perrin, P. Dillmann and A. Chaussé, *Electrochim. Acta*, 51 (2005) 745.
13. M. Cohen and K. Hashimoto, *J. Electrochem. Soc.*, 121 (1974) 42.
14. D. Kimmich, D.H. Taffa, C. Dosche, M. Wark and G. Wittstock, *Electrochim. Acta*, 202 (2016) 224.
15. I. Lozano, N. Casillas, C.P. de León, F.C. Walsh and P. Herrasti, *J. Electrochem. Soc.*, 164 (2017) D184.
16. A.J. Bard, Encyclopedia of Electrochemistry of the Elements, CRC Press, New York, 1975.
17. K.L. Hawthorne, T.J. Petek, M.A. Miller, J.S. Wainright and R.F. Savinell, *J. Electrochem. Soc.*, 162 (2015) A108.
18. D.L. Leussing and I.M. Kolthoff, *J. Am. Chem. Soc.*, 75 (1953) 2476.
19. F.J. Millero, *Geochim. Cosmochim. Acta*, 49 (1985) 547.
20. C.F. Baes and R.S. Mesmer: The Hydrolysis of Cations. John Wiley & Sons, New York, 1976.
21. B. Morgan and O. Lahav, *Chemosphere*, 68 (2007) 2080.
22. P. Montoya, T. Marín, A. Echavarría, J. A. Calderón, *Int. J. Electrochem. Sci.*, 8 (2013) 12566.
23. D. Aurbach, E. Zinigrad, Y. Cohen and H. Teller, *Solid State Ionics*, 148 (2002) 405.
24. J.W. Anthony, Handbook of Mineralogy, Mineral Data Pub, Tucson, Ariz, 1990.
25. L. Chekli, B. Bayatsarmadi, R. Sekine, B. Sarkar, A.M. Shen, K.G. Scheckel, W. Skinner, R. Naidu, H.K. Shon, E. Lombi and E. Donner, *Anal. Chim. Acta*, 903 (2016) 13.
26. A. Hazza, D. Pletcher and R. Wills, *Phys. Chem. Chem. Phys.*, 6 (2004) 1773.
27. H. D. Lim, B. Lee, Y. Zheng, J. Hong, J. Kim, H. Gwon, Y. Ko, M. Lee, K. Cho and K. Kang, *Nature Energy*, 1 (2016) 16066.

28. M. Nurullah Ates, I. Gunasekara, S. Mukerjee, E. J. Plichta, M. A. Hendrickson and K. M. Abraham, *J. Electrochem. Soc.*, 163 (2016) A2464.
29. P. G. Bruce, S. A. Freunberger, L. J. Hardwick and J.-M. Tarascon, *Nature Materials*, 11 (2012) 19.
30. A. Hazza, D. Pletcher and R. Wills, *J. Power Sources*, 149 (2005) 103.

© 2019 The Authors. Published by ESG (www.electrochemsci.org). This article is an open access article distributed under the terms and conditions of the Creative Commons Attribution license (<http://creativecommons.org/licenses/by/4.0/>).